AIAA JOURNAL
Vol. 48, No. 10, October 2010

# Acoustic Source Identification for Transitional Airfoil Flows Using Cross Correlations

Lloyd E. Jones,* Neil D. Sandham,† and Richard D. Sandberg‡
*University of Southampton, Southampton, England SO17 1BJ, United Kingdom*

DOI: 10.2514/1.J050345

**Direct numerical simulations have been conducted of the flow over NACA-0006 and NACA-0012 airfoils. For all cases multiple sources of noise have been observed. At low frequencies, the contribution of trailing-edge noise radiation is significant, while for the high frequencies, the radiated noise appears to be due only to flow events in the transition/reattachment region on the suction side. Cross correlations of acoustic and hydrodynamic quantities, combined with ray-acoustic theory, are used to identify the main source locations. While the physical origin of trailing-edge noise can be clearly identified using these methods, the situation is less clear for additional noise sources that radiate at high frequency. Evidence suggests that these additional noise sources are located downstream of transition on the suction side of the airfoil, in the region directly downstream of boundary-layer reattachment.**

## Nomenclature

| | | |
|---|---|---|
| $C_L$ | = | lift coefficient |
| $C_{pp}$ | = | correlation coefficient |
| $c$ | = | speed of sound or airfoil chord length |
| $\bar{c}_f$ | = | mean skin-friction coefficient |
| $D$ | = | computational-domain spanwise width |
| $E$ | = | total energy |
| $f$ | = | frequency |
| $M$ | = | Mach number |
| $N_\xi$, $N_\eta$ | = | number of grid points in $\xi$ and $\eta$ directions |
| $Pr$ | = | Prandtl number |
| $p$ | = | pressure |
| $p_\infty$ | = | freestream pressure |
| $p'$ | = | fluctuating part of pressure |
| $p^*$ | = | complex conjugate of pressure |
| $q_i$ | = | conduction term of the energy equation |
| $Q$ | = | second invariant of the velocity gradient tensor |
| $R$ | = | gas constant or computational-domain radius |
| $Re$ | = | Reynolds number based on airfoil chord |
| $S$ | = | variance |
| $Sr$ | = | Strouhal number |
| $T$ | = | temperature |
| $t$, | = | time |
| $u$, $v$, $w$ | = | Cartesian velocities |
| $u_\infty$ | = | freestream velocity |
| $W$ | = | computational-domain wake length |
| $x$, $y$, $z$ | = | Cartesian coordinates |
| $\alpha$ | = | airfoil incidence |
| $\gamma$ | = | ratio of specific heats |
| $\Delta t$ | = | time-step |
| $\delta_{ij}$ | = | Kronecker delta |
| $\mu$ | = | dynamic viscosity |
| $\xi$, $\eta$ | = | curvilinear wall-tangential and wall-normal coordinates |
| $\rho$ | = | density |
| $\sigma$ | = | standard deviation |
| $\tau_{ij}$ | = | shear-stress tensor |

Received 27 November 2009; revision received 19 May 2010; accepted for publication 4 June 2010. 

*Research Fellow, School of Engineering Sciences; ljones@soton.ac.uk. Member AIAA.

†Professor, School of Engineering Sciences; n.sandham@soton.ac.uk. Senior Member AIAA.

‡Lecturer and RAEng/EPSRC Research Fellow, School of Engineering Sciences; sandberg@soton.ac.uk. Senior Member AIAA.

## I. Introduction

WHEN considering airfoil self-noise most studies focus upon trailing-edge noise. Indeed, Brooks et al. [1] classified five mechanisms for airfoil self-noise, all but one of which have noise generated mainly by the interaction of disturbances with the airfoil trailing edge. It is therefore usual to consider only trailing-edge noise for the purposes of airfoil self-noise prediction. An important example is Amiet's classical theory [2] for trailing-edge noise, which is widely used for the design of airfoils [3,4]. Amiet's theory predicts the far-field noise produced by the turbulent flow over an airfoil, using only the airfoil surface pressure difference as input, and assumes that all noise is generated at the airfoil trailing edge. Recently, the presence of additional noise sources distinct from sources at the airfoil trailing edge has been observed. In a two-dimensional numerical study, Tam and Ju [5] observed that vortices in the airfoil wake may themselves generate pressure waves, via a mechanism independent of the airfoil trailing edge. In a three-dimensional numerical study of an airfoil at incidence exhibiting a separation bubble, Sandberg et al. [6] observed the transition/reattachment region to act as a source of noise distinct from the airfoil trailing edge, possessing markedly different directivity. Similar behavior was observed in two dimensions [7], in which the nature of the simulation prevented the development of turbulence. Furthermore, it is known that the leading edge of the airfoil may produce a backscattering effect, particularly for low frequencies [8]. Since these noise-production mechanisms are distinct from that occurring at the trailing edge, they will not be predicted correctly by classical methods based upon surface pressure difference (e.g., Amiet's theory [2]). Clearly determining the nature and significance of noise sources other than the trailing edge is therefore important for accurate airfoil self-noise prediction.

Continued advances in computing power mean that direct numerical simulation (DNS) of airfoil flows for the purposes of investigating aeroacoustic behavior is now possible. Compressible DNS is capable not only of accurately representing hydrodynamic phenomena such as turbulence and transition to turbulence, but also hydrodynamic noise-production mechanisms and the propagation of acoustic waves. The hydrodynamic and acoustic behavior can be computed directly with no modeling and with no interfacing between solution methods, as is required for hybrid approaches. Early DNS of airfoil flows were limited to either two dimensions [9,10] or else did not resolve transition [11]. Despite the preclusion of turbulence, two-dimensional simulations have proven useful in studying several aspects airfoil self-noise including the role of wake-vortices in noise

production [5], the accuracy of Amiet's theory for predicting self-noise for finite-thickness airfoils [7] and mechanisms behind tonal airfoil self-noise [12]. The first turbulent airfoil DNS was performed by Shan et al. [13], who investigated the effect of pulsed jets as a flow control measure. Jones et al. [14] later performed a study of an airfoil with a laminar separation bubble and determined that the observed turbulence would self-sustain via a three-dimensional absolute instability, for which a mechanism was proposed. Jones et al. employed a compressible code and also resolved the acoustic field; hence, the accuracy of Amiet's theory for predicting airfoil self-noise from a three-dimensional flow could also be investigated [6]. It was determined that for the flow in question, which exhibited multiple acoustic sources, Amiet's theory would not be able to accurately predict trailing-edge noise. In recent years large eddy simulation (LES) has become increasingly favored for aeroacoustic studies. Because of the decreased computational expense it is possible to compute higher-Reynolds-number airfoil flows than are achievable with DNS. For example, the tonal airfoil noise phenomenon has been investigated [15] at Reynolds number $1 \times 10^5$ and airfoil trailing-edge noise has been computed successfully [16] at Reynolds number $5 \times 10^5$. The computational expense of LES as a tool for airfoil aeroacoustic predictions can be reduced further by coupling to a second, less computationally expensive, method to solve for the acoustic far field. For example, LES can be used to provide the source terms for an acoustic analogy [15,17] or can be employed to directly compute the near-field acoustics before propagating to the far field by a second numerical method [18,19]. The modeling procedures inherent in LES make it less suitable for fundamental research, however: in particular, for flows where accurately capturing transition is important and a priori knowledge of the transition location is not available. For such circumstances, DNS remains the preferred research tool.

The aim of this numerical study is therefore to investigate the relationship between the acoustic and hydrodynamic fields of transitional flows over airfoils exhibiting multiple noise sources. This will be performed by conducting DNS of transitional airfoil flows that allow investigation of both the hydrodynamic and acoustic behavior of the flow. The relationship between the acoustic and hydrodynamic behavior will then be investigated by cross correlations in conjunction with acoustic ray theory. This causality method has been employed in many experimental studies to identify acoustic sources for jet noise; for a summary of these studies, see Bogey and Bailly [20], who also employed the causality method in a numerical study of jet noise. The method is chosen in preference to, for example, numerically evaluating a beamforming algorithm, due to the significantly reduced complexity of the method and a clear-cut physical interpretation.

## II. Governing Equations

The DNS code directly solves the unsteady compressible Navier–Stokes equations, written in nondimensional form as

$$\frac{\partial \rho}{\partial t} + \frac{\partial}{\partial x_k}(\rho u_k) = 0 \tag{1}$$

$$\frac{\partial}{\partial t}(\rho u_i) + \frac{\partial}{\partial x_k}[\rho u_i u_k + p\delta_{ik} - \tau_{ik}] = 0 \tag{2}$$

$$\frac{\partial}{\partial t}(\rho E) + \frac{\partial}{\partial x_k}[u_k(\rho E + p) + q_k - u_i \tau_{ik}] = 0 \tag{3}$$

where the total energy is defined as $E = T/[\gamma(\gamma-1)M^2] + 0.5u_i u_i$. The stress tensor and the heat-flux vector are computed, respectively, as

$$\tau_{ik} = \frac{\mu}{Re}\left(\frac{\partial u_i}{\partial x_k} + \frac{\partial u_k}{\partial x_i} - \frac{2}{3}\frac{\partial u_j}{\partial x_j}\delta_{ik}\right), \qquad q_k = \frac{-\mu}{(\gamma-1)M^2 PrRe}\frac{\partial T}{\partial x_k} \tag{4}$$

where the Prandtl number is assumed to be constant at $Pr = 0.72$ and $\gamma = 1.4$. The molecular viscosity $\mu$ is computed using Sutherland's law [21], setting the ratio of the Sutherland constant over freestream temperature to 0.36867. To close the system of equations, the pressure is obtained from the nondimensional equation of state $p = (\rho T)/(\gamma M^2)$. The primitive variables $\rho$, $u_i$, and $T$ have been nondimensionalized by the freestream conditions and the airfoil chord is used as the reference length scale. Dimensionless parameters $Re$, $Pr$, and $M$ are defined using freestream (reference) flow properties.

## III. Direct Numerical Simulations

### A. Numerical Method

Fourth-order-accurate central differences using a five-point stencil are used for the spatial discretization, with fourth-order accuracy extended to the domain boundaries by means of a Carpenter boundary scheme [22]. No artificial viscosity or filtering is used. Instead, stability is enhanced by appropriate treatment of the viscous terms in combination with entropy splitting of the inviscid flux terms [23]. An explicit fourth-order-accurate Runge–Kutta scheme is used for time stepping. The code is based upon an existing code that has been previously validated for compressible turbulent-plane channel flow [23] and, more recently, has been demonstrated to accurately represent the development of hydrodynamic instabilities [24]. The code used in the current study is different in that it is applied to a curvilinear C-type grid with wake connection; however, the same metric terms were used in previous versions of the code. The topology of the curvilinear C-grid used is given in Fig. 1. At the freestream boundary $\eta^+$, where the only disturbances likely to reach the boundary will be in the form of linear waves, an integral characteristic boundary condition is applied [25], in addition to a sponge layer comprising a dissipation term added to the governing equations. At the downstream exit boundary $\xi^{\pm}$, which will be subject to the passage of nonlinear fluid structures, a zonal characteristic boundary condition [26] is applied for increased effectiveness. At the airfoil surface, an adiabatic no-slip condition is applied, and for three-dimensional simulations, a periodic boundary condition is applied in the spanwise ($z$) direction.

### B. Grid Resolution and Domain Size

The influence of domain size and grid resolution have been investigated thoroughly for the flow around a NACA-0012 airfoil at $Re = 5 \times 10^4$ and $\alpha = 5°$ in Jones et al. [14], and only a selection of results is included here. For completeness, the simulation at $\alpha = 5°$ discussed here is that referred to as case 3DU in Jones et al. [14].

#### 1. *Two-Dimensional Analysis*

Resolution requirements for DNS of the flow around an airfoil at incidence are complex, since a variety of fluid phenomena are present

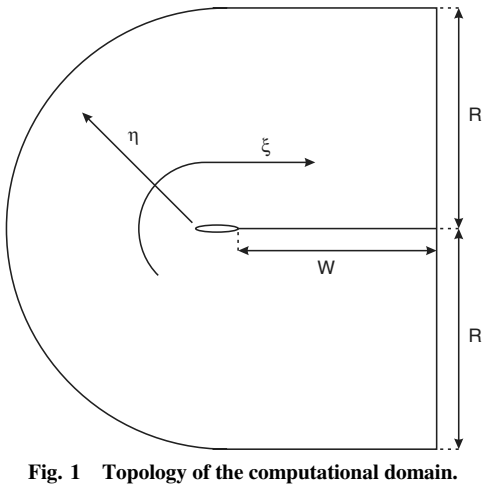


**Fig. 1 Topology of the computational domain.**

**Table 1 Domain and grid dimensions for grid resolution investigation at $Re_c = 5 \times 10^4$, $\alpha = 5°$**

| Grid | G1 | G2 | G3 |
|---|---|---|---|
| $R$ | 5.3 | 5.3 | 7.3 |
| $W$ | 5 | 5 | 5 |
| $N_\xi$ | 2001 | 2570 | 2570 |
| $N_\eta$ | 440 | 440 | 692 |
| $N_{\text{foil}}$ | 541 | 1066 | 1066 |
| $N_{\text{wake}}$ | 1462 | 1506 | 1506 |

and must be resolved. Grid generation is therefore achieved by an iterative approach. Since the numerical code possesses low dissipation, the presence of underresolved flow phenomena results in numerical oscillations, particularly in sensitive quantities such as density gradient. By analyzing simulation results, locations of poor resolution may be identified, and a new grid may be generated in order to improve resolution in the necessary locations. The flowfield data are then interpolated onto the new grid and the simulation is continued. The iterative grid production process is documented here for the flow around a NACA-0012 airfoil at $\alpha = 5°$. Simulations were run on three grids in total, with details given in Table 1.

When run in two dimensions, the upper airfoil boundary layer is observed to separate near the leading edge of the airfoil. The separated shear layer subsequently rolls up to form vortices, and periodic vortex shedding is observed (Fig. 2, grid G3). The system of laminar separation, shear-layer roll-up, and periodic vortex shedding causes the lift coefficient to oscillate (Fig. 3, left). When run using grid G1, $C_L$ oscillates in an almost perfectly periodic fashion. Some evidence of numerical oscillation was observed when isocontours of vorticity were plotted at sensitive levels; hence, grid G2 was generated with an increased streamwise grid resolution over the airfoil surface. When the simulation was continued on grid G2, the mean $C_L$ increased, and the time-dependent behavior became slightly less regular. Numerical oscillations could no longer be observed in hydrodynamic properties; however, the fundamental frequency of the vortex shedding remained unchanged. When the simulation was continued on grid G3 minimal difference was observed in $C_L$. It appears that grid G2 adequately captures the vortex-shedding behavior observed in two dimensions, with no evidence of underresolution. Grid G3 is more suited to three-dimensional simulations, however, since the increased wall-normal resolution is more appropriate for resolving turbulence.

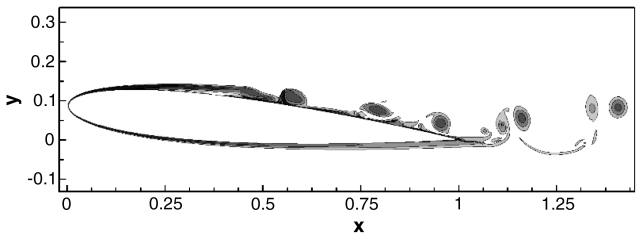


**Fig. 2 Isocontours of vorticity for the two-dimensional flow around a NACA-0012 airfoil at $Re = 5 \times 10^4$ and $\alpha = 5°$, showing 20 levels over the range ±150, computed using grid G3.**

The effect of altering domain size may also be investigated by considering simulations run using grids G2 and G3; grid G2 is of radius $R = 5.3$, whereas grid G3 has a radius of $R = 7.3$. The azimuthal variation of $p/p_\infty$, where $p_\infty$ is the freestream pressure, is plotted in Fig. 3 (right) for both grids, at a radius of three chords from the airfoil trailing edge. At around 0° there is a difference of approximately $1.5 \times 10^{-3}$ between normalized pressure for the two grids, presumably caused by differences in resolution in the $\eta$ direction in the wake region; however, this is the only significant difference observed. The azimuthal pressure distribution in the potential flow region appears remarkably similar for both cases, and the difference between grids in this region is significantly less than $p/p_\infty = 1 \times 10^{-3}$. If the radius of the domain were increased beyond seven chords, further changes would be even smaller in amplitude. It appears then that a domain radius of 5.3 airfoil chords adequately captures the potential flow about the airfoil; hence, the chosen domain radius of 7.3 chords is more than adequate.

### 2. *Three-Dimensional Analysis*

Using $\bar{c}_f$ predictions from XFoil [27], the grid resolution over the aft section of the airfoil for grid G3 was compared to turbulent-plane channel-flow data [23], which suggested that grid G3 would be adequate for three-dimensional simulations. The spanwise domain width was then selected based upon criteria determined from simulations of the flow over a backward-facing step [28]; a domain width of $D = 0.2$ was chosen, being 9.6 times the maximum bubble height of $\delta^* = 2.09 \times 10^{-2}$ and 7.2 times $\delta^*$ at the trailing edge. The number of spanwise grid points was chosen to be 96, again based on the resolution requirements of turbulent-plane channel flow and $\bar{c}_f$ predictions via XFoil. During the initial stages of three-dimensional simulations, flowfield properties were checked in order to confirm that all fluid structures appeared resolved. A final confirmation of adequate spatial and temporal resolution is provided by a posteriori statistical analysis. Grid resolution in wall units, taken at the maximum turbulent $\bar{c}_f$ location observed within the turbulent region, was found to differ slightly from XFoil predictions, but was still found to be well resolved based on turbulent-plane channel-flow criteria. Resolution in wall units, taken at $x = 0.72$ where the maximum $\bar{c}_f$ of $7.60 \times 10^{-3}$ is observed, is given in Table 2. Finally,

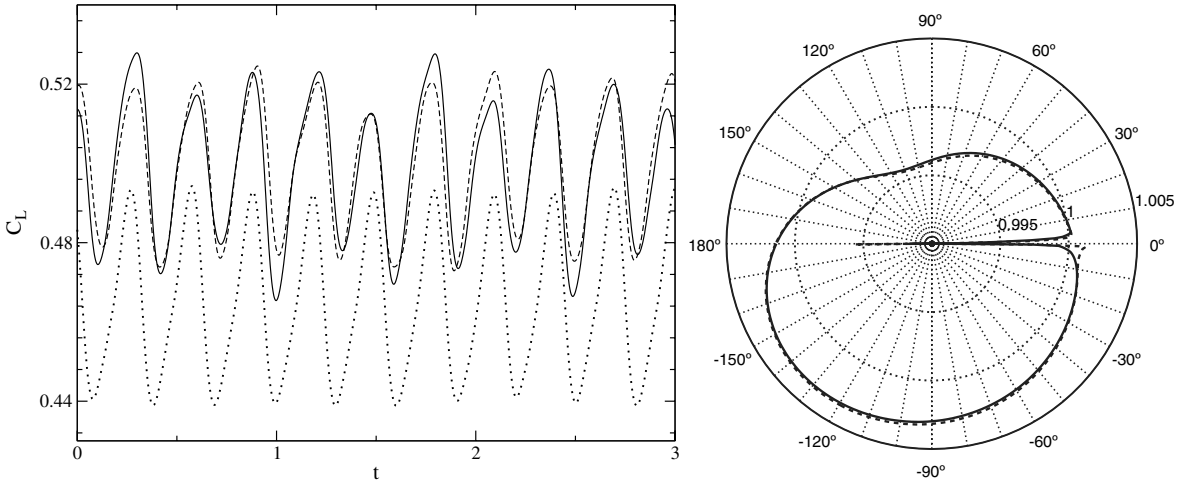


**Fig. 3 Left-hand image shows time-dependent $C_L$ for grids G1 (dotted line), G2 (dashed line) and G3 (solid line). Right-hand image shows azimuthal variation of $p/p_\infty$ over the range 0.99 to 1.005, at three chords (right) radius from the airfoil trailing edge, for grids G2 (dashed line) and G3 (solid line).**

**Table 2 Grid resolution in wall units at the maximum $\bar{c}_f$ location for the three-dimensional flow around a NACA-0012 airfoil at $Re = 5 \times 10^4$ and $\alpha = 5°$**

| Simulation | $\Delta x^+$ | $\Delta z^+$ | $\Delta y^+$ | $N_\eta$: $y^+ < 10$ |
|---|---|---|---|---|
| NACA-0012 airfoil at $Re = 5 \times 10^4$, $\alpha = 5°$ | 3.12 | 6.02 | <1.0 | 10 |
| Sandham et al. [23] | 15 | 7.5 | - | 10 |

in order to confirm that turbulent behavior is resolved over all time and length scales, spanwise and temporal turbulent kinetic energy (TKE) spectra were computed [14] and found to exhibit roll-off of $10^3$ and $10^6$, respectively, comparing favorably with reference boundary-layer DNS [29].

### C. Results and Discussion

Direct numerical simulations were conducted of the compressible flow around a NACA-0006 airfoil at $\alpha = 7°$ and a NACA-0012 airfoil at $\alpha = 5°$ and $\alpha = 7°$ for a Reynolds number based on chord of $Re_c = 5 \times 10^4$ and $M = 0.4$. Computational grids for the simulations at $\alpha = 7°$ were generated using the same method as given in Sec. III.B, comparing to the same turbulent channel reference data. For all simulations the computational domain possessed dimensions as specified for grid G3 in Table 1 and spanwise domain width $D = 0.2$. The computational domains are discretized using $2570 \times 692$ and $2587 \times 692$ nonequidistantly spaced points in the lateral and normal directions for $\alpha = 5$ and 7°, respectively, resulting in a total of approximately $1.7 \times 10^8$ points. The nondimensional time step was set to $1.4 \times 10^{-4}$ to satisfy numerical stability criteria of the explicit time-marching scheme; hence, frequencies up to $f \approx 350$ will be resolved with more than 20 steps per wavelength. This compares to frequencies of $f \approx 8.5$ for the most amplified hydrodynamic instability waves of the NACA-0012 case at $\alpha = 5°$ [30]. Simulations are progressed until a statistically stationary state is achieved (approximately $t = 8.4$), before capturing statistics over an interval of $\Delta t = 7.7$, with sampling frequency $\Delta t = 1 \times 10^{-3}$ (every 10 iterations). At $t = 0$ each three-dimensional simulation is subject to a perturbation in $\rho u_i$ of order $1 \times 10^{-3}$, located within the boundary layer at $x = 0.2$. The perturbation extends over a region of $3 \times 3$ grid points in the $\xi$ and $\eta$ directions and possesses a random amplitude distribution in the $z$ direction. The intention is to excite absolute instability mechanisms within the separation that will lead to self-sustaining turbulence. No further disturbances are added; the simulations are progressed in time and in each case the laminar–turbulent transition self-sustains, following the mechanism identified in Jones et al. [14].

The code used is a variant of the in-house SBLI DNS code, which has been found to scale with near perfect efficiency to 168,000 processor cores on the ORNL Jaguar cluster. Simulations were conducted using national supercomputer facilities HECToR and HPCx. Simulations performed on HECToR used 1024 processor cores (AMD Opteron 2.3 Ghz, eight cores per node with 8 Gb shared memory), for a total of approximately 138 h.

#### 1. *Instantaneous Flow and Acoustic Fields*

The acoustic response of the flow over the airfoil is highly dependent on the hydrodynamic behavior. In Fig. 4, isosurfaces of $Q = 100$, colored by the streamwise vorticity component illustrate the respective flow patterns. The flow around the NACA-0012 airfoil at $\alpha = 5°$ separates from the upper airfoil surface due to the presence of an adverse pressure gradient, at approximately $x = 0.10$. The separated shear layer undergoes transition to turbulence and, due to the subsequent increase in wall-normal momentum transfer,

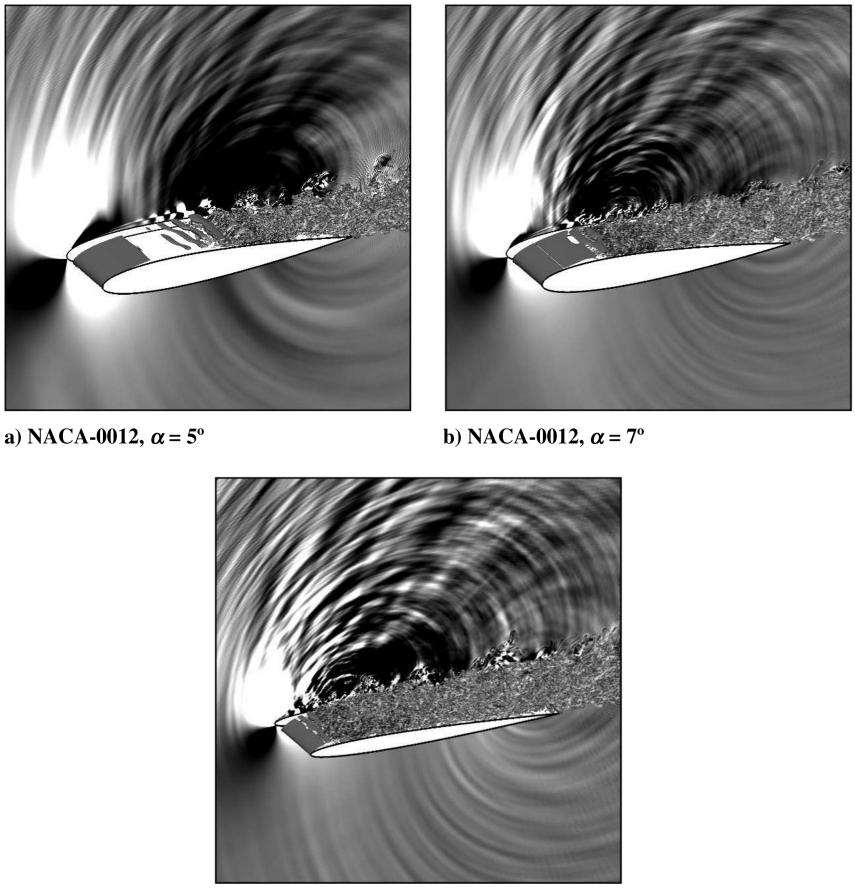

**a) NACA-0012, $\alpha = 5°$** **b) NACA-0012, $\alpha = 7°$**

**c) NACA-0006, $\alpha = 7°$**

**Fig. 4 Instantaneous isosurfaces of $Q = 100$, with instantaneous contours of dilatation rate in range $[-0.05; 0.05]$ for the case at $\alpha = 5°$ and $[-0.1; 0.1]$ for cases at $\alpha = 7°$.**

reattaches as a turbulent boundary layer at $x \approx 0.61$. This long separation bubble with laminar–turbulent transition taking place far downstream of the leading edge was identified previously to generate additional noise sources that are not included in classical trailing-edge theories [6]. Increasing the angle of attack to $\alpha = 7°$ results in a significantly faster laminar–turbulent transition process and an earlier turbulent reattachment at $x = 0.39$. The thinner airfoil at $\alpha = 7°$ shows an even shorter separation bubble with a developing turbulent boundary layer extending from approximately $x = 0.10$ to the trailing edge. For all cases, on the lower airfoil surface the pressure gradient is favorable for much of the airfoil chord; hence, at this comparatively low Reynolds number, the boundary layer remains laminar.

The main objective of the current research is to investigate airfoil self-noise. It is therefore essential that noise generated by the airfoil is represented accurately by the simulation. In particular, reflections from the boundaries must not interfere with, or even overpower, the low-amplitude airfoil self-noise. Instantaneous contours of dilatation rate at the plane $z = 0.1$, shown in Fig. 4, illustrate the sound waves originating from the airfoil flow. The zonal characteristic boundary condition is able to sufficiently reduce reflections due to the wake structures passing through the outflow boundary. Pressure fluctuations associated with trailing-edge noise are expected to exhibit a symmetric wave pattern with respect to $y = 0$, with predominantly upstream directed sound radiation and a phase difference of 180° between radiation above and below the airfoil, as observed for flat-plate studies [24], and the wave pattern should originate close to the trailing edge. For all current cases, it is apparent that sound radiation below and above the airfoil is highly disparate. On the bottom side, the radiated sound appears to only originate from the trailing edge, while on the top side multiple sources seem to be present, similar to the previous two-dimensional study [24]. For cases with turbulent reattachment locations further upstream, the origin of the sound waves observed above the airfoil (excluding trailing-edge sources) is also further upstream, indicating that the additional noise sources are associated with turbulent reattachment.

### 2. *Acoustic Fields in the Frequency Domain*

From instantaneous contours of dilatation rate (Fig. 4), it was observed that sound radiation is highly asymmetric with respect to the chord line. However, scrutinizing data in the time domain does not reveal whether the asymmetry is present for the entire frequency range or whether there are particular frequencies that cause this type of radiation pattern. The data were therefore transformed to the frequency domain using one-third-octave averaging about several target frequencies to account for the broadband nature of the airfoil self-noise. The modulus of pressure for nondimensional target frequencies is shown in Figs. 5–9 for the NACA-0012 airfoil at $\alpha = 5°$. The reference length and velocity scales for the cases under consideration are the airfoil chord and freestream velocity, respectively; hence, the nondimensional frequency $f$ is equivalent to a Strouhal number $Sr = fc/u_\infty$.

The frequencies have been chosen to correspond to different hydrodynamic and acoustic phenomena for each flow configuration. The lowest frequency in each case lies below the frequency of the most strongly amplified convective instabilities [31] and corresponds to the frequency of the vortex shedding observed in two-dimensional studies of the same airfoil configuration [7]. The frequency $f = 7.75$ is chosen to lie directly within the range of frequencies expected to be strongly amplified within the separated shear layer via convective instability [31]. The highest frequency selected ($f = 15$) is higher

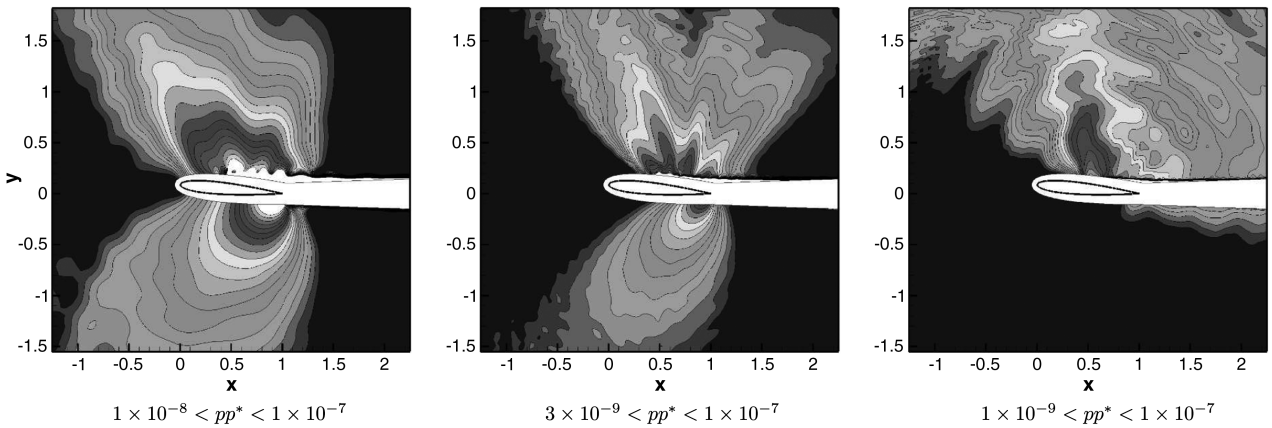


**Fig. 5 Isocontours of $pp^*$ employing one-third-octave averaging, centered about $f = 3.37$, $f = 7.75$, $f = 15$ (from left to right) using 20 levels exponentially distributed over different ranges; NACA-0012 at $\alpha = 5°$.**

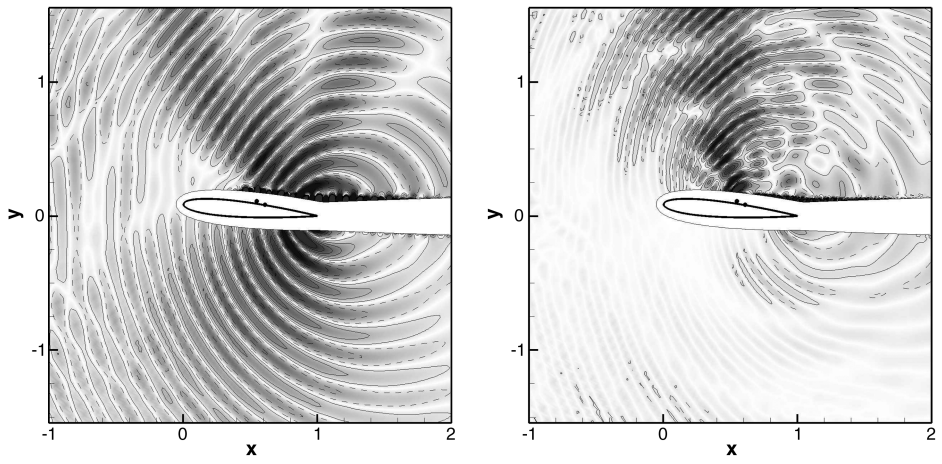


**Fig. 6 Isocontours of the real part of acoustic pressure plotted for $f = 7.75$ (left) and $f = 15$ (right) for the NACA-0012 airfoil at $\alpha = 5°$. Black circles indicate the location of maximum TKE and the mean reattachment point.**

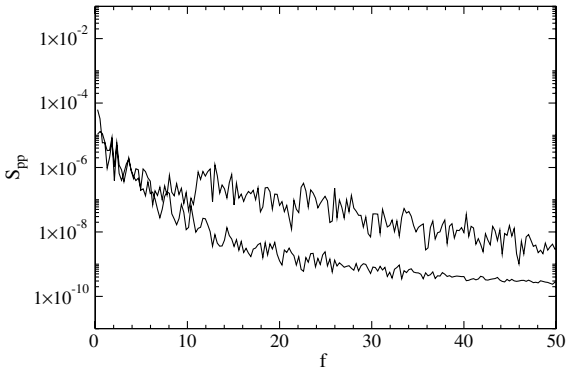


**Fig. 7 Pressure power-spectra computed at locations $(x, y)$= $(0.5, 0.5)$ (upper curve) and $(x, y) = (0.5, -0.5)$ (lower curve) for the NACA-0012 airfoil at $\alpha = 5°$.**

than that associated with the most amplified convective instabilities [31]. Additionally, at $f = 15$ pressure fluctuations over the lower airfoil surface were limited to very near the airfoil trailing edge [31], suggesting that acoustic scattering is not efficient at this frequency.

For the NACA-0012 case at $\alpha = 5°$, the frequency corresponding to the vortex shedding of the matching two-dimensional simulation was $f = 3.37$, shown in Fig. 5 (left). For this one-third-octave-averaged frequency, the behavior of the radiated pressure is consistent with trailing-edge noise, i.e., showing an origin at the trailing edge with a high degree of symmetry about the airfoil chord. Nevertheless, there appears to be an additional lobe radiating upstream on the suction side, indicating that at this frequency there is an additional noise source. The one-third-octave-averaged pressure modulus at $f = 7.75$ displays significant noise radiation from the trailing edge, although the radiation pattern above the airfoil displays strong modulation most likely due to interference with noise radiated from additional sources. At the highest frequency considered (Fig. 5, right), the largest-amplitude pressure fluctuations are present only above the airfoil and clearly do not originate at the airfoil trailing edge. Figure 6 shows the real part of acoustic pressure for individual frequencies, illustrating the wave fronts associated with acoustic propagation. The origin of the acoustic waves is difficult to determine to a high degree of accuracy, but appears to lie downstream of $x = 0.5$ for high frequencies. A crude estimate of the source location $x_s$ based on visually tracking wave fronts is determined to be $0.6 < x_s < 0.7$. The hydrodynamic nature of this secondary source is not clear. However, given that acoustic waves appear to originate in the transition/reattachment region close to the airfoil surface, it seems possible that fluctuating surface shear-stress components could be an important source of acoustic radiation, as found for turbulent channel flow at low Mach numbers by Hu et al. [32]. The contribution of the additional noise sources to the total airfoil self-noise can be assessed by computing pressure spectra above and below the airfoil at $(x, y) = (0.5, \pm 0.5)$, as shown in Fig. 7. Spectra were obtained by splitting the pressure time series into three segments overlapping by 50%, before applying Hanning windowing and ensemble averaging the segmented spectra. For frequencies $f < 6$ the spectra appear similar above and below the airfoil, whereas for frequencies $f > 10$ the spectrum obtained above the airfoil is significantly greater in amplitude. This suggests that for frequencies $f < 6$ the airfoil trailing edge is the dominant noise source, whereas for $f > 10$ the additional sources are dominant. It is also apparent that the trailing-edge noise is greatest in amplitude at very low frequencies, including frequencies lower than that of the vortex shedding ($f = 3.37$ for the case at

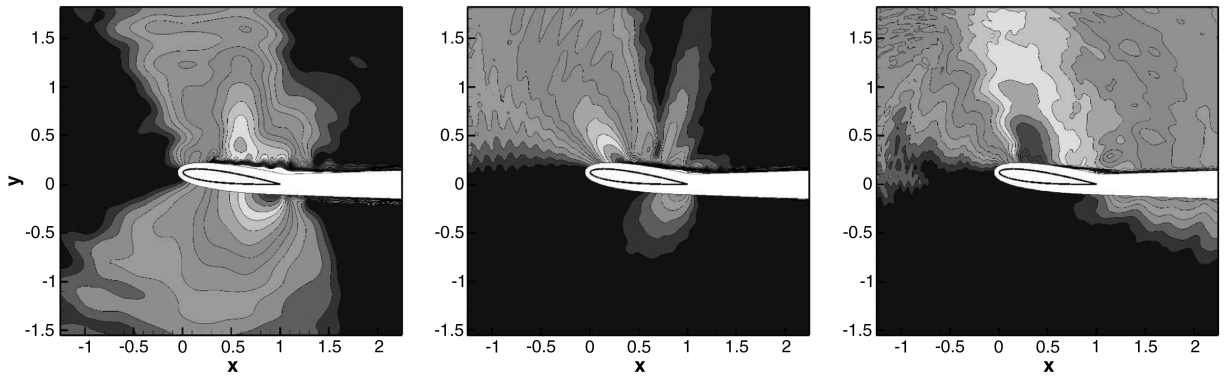


**Fig. 8 Isocontours of $pp^*$ employing one-third-octave averaging, centered about $f = 2.5, 7.75$, and 15 (from left to right) using 20 levels exponentially distributed over different ranges; NACA-0012 at $\alpha = 7°$.**

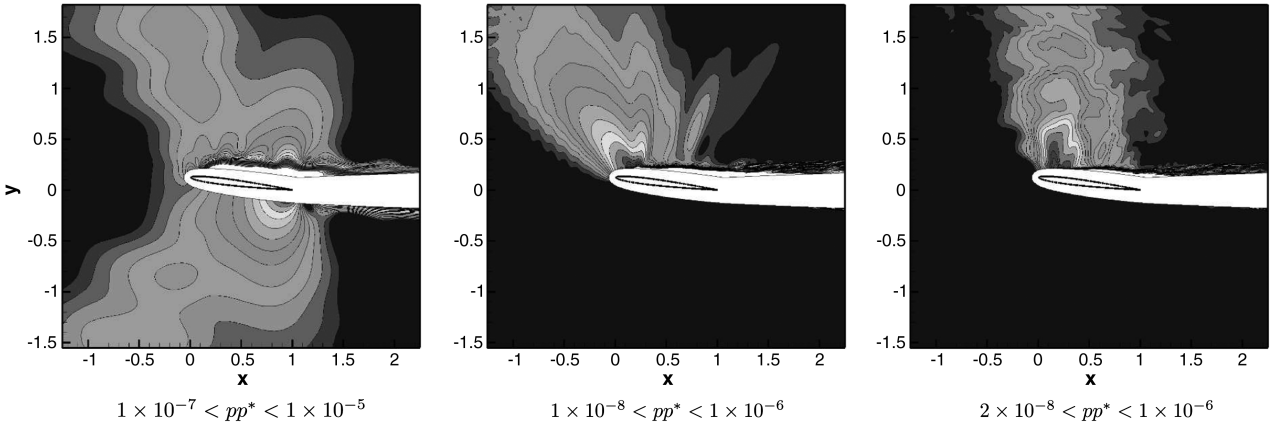


**Fig. 9 Isocontours of $pp^*$ employing one-third-octave averaging, centered about $f = 3.37, 7.75$, and 15 (from left to right) using 20 levels exponentially distributed over different ranges; NACA-0006 at $\alpha = 7°$.**

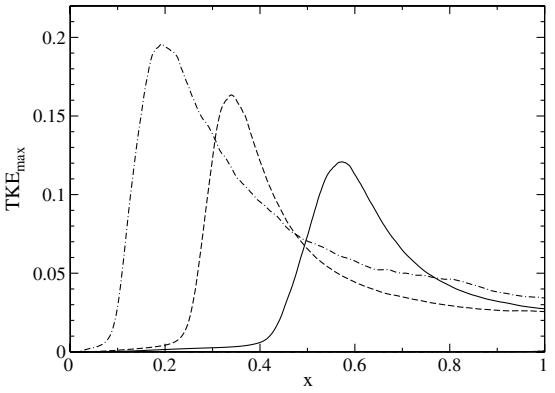


**Fig. 10 The maximum TKE observed within the upper-surface boundary layer plotted as a function of $x$ for the NACA-0012 airfoil at $\alpha = 5°$ (solid line), the NACA-0012 airfoil at $\alpha = 7°$ (dashed line) and the NACA-0006 airfoil at $\alpha = 7°$ (dotted–dashed).**

$\alpha = 5°$). The presence of low-frequency disturbances is not unexpected for separation-bubble flows (e.g., [33,34]) and hence is not surprising for the current case, in which the periodic two-dimensional vortex shedding becomes intermittent for the turbulent flow. Although the turbulent flow over the trailing edge is essentially broadband, trailing-edge scattering is more efficient at low frequencies; hence, they appear more prominent. The computational expense of DNS prohibits the capture of time series sufficient to analyze very-low-frequency behavior, however; hence, the low-frequency range will not be studied in detail.

Increasing the angle of attack of the NACA-0012 case to $\alpha = 7°$ does not qualitatively change the picture, as evidenced by Fig. 8. For low frequencies, the contribution of trailing-edge noise radiation is significant, while for the highest frequency investigated, the radiated noise appears to be due only to the flow events in the transition/reattachment region on the suction side. However, for $f = 7.75$, noise is radiated from the transition/reattachment region at a considerably higher amplitude than for the case at smaller incidence. For the thinner NACA-0006 airfoil, shown in Fig. 9, higher amplitudes of $pp^*$ are observed for all frequency ranges, indicating that airfoil self-noise is radiated more efficiently for this case. This was unexpected, as it was assumed that the thin-airfoil case, due to its rapid laminar–turbulent transition process, would show the least remnants of transitional effects and spanwise coherence would be reduced versus the cases with long separation bubbles, resulting in reduced noise levels. However, in contrast to the NACA-0012 cases, most of the radiated noise originates from the transition/reattachment location and a significant trailing-edge noise contribution can only be observed at the lowest frequency.

The amplitude of the additional noise sources is greatest for the for the NACA-0006 airfoil at $\alpha = 7°$ and least for the NACA-0012 airfoil at $\alpha = 5°$. Therefore, from this small sample, it appears that the amplitude of the additional noise sources increases with the strength of the adverse pressure gradient, and hence with increasing convective instability growth rates, in the separated region. The maximum TKE observed within the boundary layer for the NACA-0006 airfoil at $\alpha = 7°$ was 0.19 (Fig. 10), whereas for the NACA-0012 airfoils at $\alpha = 7$ and 5° the maximum TKEs were 0.16 and 0.11, respectively, providing evidence that the amplitude of the additional noise sources is related to that of the turbulent fluctuations in the transition region.

## IV. Cross Correlations for Source Identification

Visual inspection of Figs. 5–9 suggests that, for certain frequencies, most of the radiated noise originates from the transition/reattachment region. To investigate the location and nature of the additional sources acoustic pressure fluctuations in the far field were cross-correlated with the hydrodynamic behavior in the vicinity of the airfoil. A cross correlation $C_{fp}$ is computed between a hydrodynamic variable of interest $f$ (e.g., $u$ velocity or pressure) taken at some point on or near the surface of the airfoil, denoted as a source location $(x_s, y_s)$ at time $t$, and the pressure $p$ taken at some point in the far field, denoted as an observer location $(x_o, y_o)$ at time $t + \Delta t_{ac}$ as

$$C_{fp} = \frac{S_{fp}}{\sigma_f \sigma_p} \tag{5}$$

where $\sigma$ signifies the standard deviation (or root mean square) of a function, and $S$ is the covariance.

For a given source and observer location, $(x_s, y_s)$ and $(x_o, y_o)$, respectively, the time taken for an acoustic wave propagating from the source location to the observer location can in principle be calculated. Equation (5) can then be solved specifying $\Delta t_{ac}$ to correspond to the propagation time, allowing direct correlation between the acoustic field and the hydrodynamic field. To determine the propagation time a simple ray-propagation technique is employed. The method does not account for refraction effects due to changes in sound speed; however, such effects are expected to be small at $M = 0.4$. In the current case, the mean sound speed exhibits a maximum deviation less than 3% from the freestream value. Ray-acoustics theory [35], accounting for refraction effects, was applied to the case of flow over a NACA-0012 airfoil at $\alpha = 5°$, showing no significant differences compared to the simplified ray-propagation method. Hence, due to the smaller computational expense, all results presented in the current paper were obtained using the simplified technique.

The time and spanwise averaged flowfield of the airfoil configuration of interest is considered. Given a source location $(x_s, y_s)$ with local velocity components $u_s$, $v_s$, and temperature $T_s$, the path of an acoustic ray with initial propagation vector $\theta$ may be computed as follows. The acoustic ray will propagate at $c_s = \sqrt{T}/M$, with Cartesian velocity components $c_x = c_s \cos\theta$ and $c_y = c_s \sin\theta$. After a small time $\Delta t$ the acoustic ray will have propagated a distance $\Delta x = \Delta t(u_s + c_s \cos\theta)$ and $\Delta y = \Delta t(u_s + c_s \sin\theta)$. The acoustic perturbation will now be located at $(x_1, y_1) = (x_s + \Delta x, y_s + \Delta y)$, with associated fluid properties $u_1$, $v_1$, and $T_1$. Repeating the process to compute new values of $c_x$ and $c_y$ and integrating in time recovers a trajectory (or ray) that describes the path of a point on an acoustic wave front. For each point on the trajectory $\sum \Delta t$ is known; hence, the time taken for an acoustic wave to propagate to that location is known. This is illustrated in Fig. 11 (left) for a range of $\theta$ originating at a source location within the upper-surface boundary layer at $x_1 = -0.5$.

To solve Eq. (5) to yield meaningful results for given source and observer locations $(x_s, y_s)$ and $(x_o, y_o)$, we need to determine the acoustic-propagation angle $\theta$ that results in a ray passing through the point $(x_o, y_o)$ and the time taken for an acoustic wave to propagate along this trajectory. To perform this the secant method is employed. For given source and observer locations $(x_s, y_s)$ and $(x_o, y_o)$, trajectories are computed while varying $\theta$ until a trajectory passing within a user specified distance to point $(x_o, y_o)$ is recovered. This has been performed for a variety of streamwise positions in order to produce rays passing through the point $(x_o, y_o) = (0.5, 1.0)$ and is plotted in Fig. 11 (right). For each source location the time taken for an acoustic wave to propagate to the observer location is known, and cross correlations can be computed for this $\Delta t_{ac}$. This value of $\Delta t_{ac}$ is computed from mean flow data, and in the time-dependent flow the inherently unsteady behavior present will mean that the propagation time will vary about this mean.

Given that the airfoil flows exhibit markedly different acoustic behavior depending upon the frequency range considered, it is desirable to perform cross correlations in the frequency domain for a range of frequencies. To achieve this the pressure time series for the source and observer locations are first Fourier transformed in time. Frequencies that lie outside the range of interest are then discarded, and the pressure signal is reconstructed by computing a reverse Fourier transform of the remaining modes. An example of pressure signals computed for finite-frequency ranges is plotted in Fig. 12. The cross correlations presented here are computed from acoustic and hydrodynamic pressure obtained from the airfoil midspan plane.

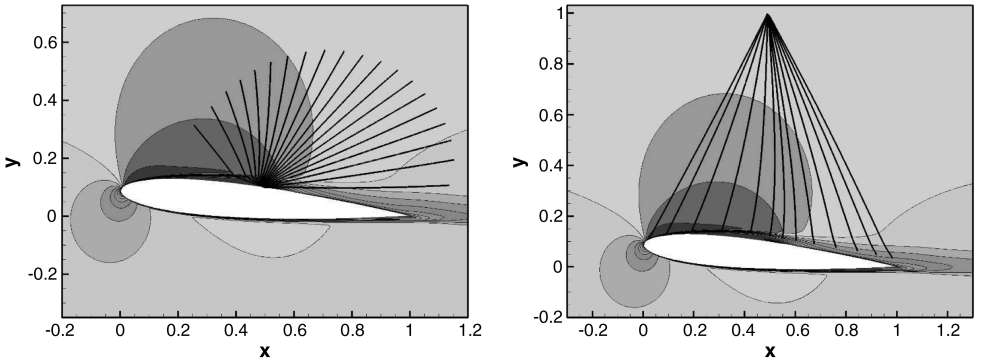


**Fig. 11 Left-hand image shows acoustic-propagation rays computed for a variety of wave angles originating at $x = 0.5$ within the upper-surface boundary layer, rays were integrated to $t = 0.2$ using time step $\Delta t = 1 \times 10^{-3}$. Right-hand image shows acoustic-propagation rays for a variety of source locations within the upper-surface boundary layer, with wave angle specified such that each ray passes through the point $(x_o, y_o) = (0.5, 1.0)$; NACA-0012 at $\alpha = 5°$.**

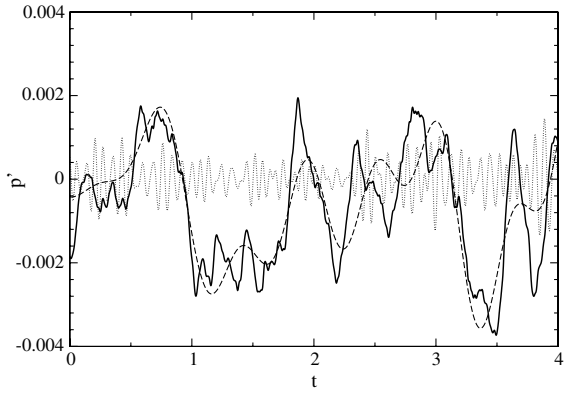


**Fig. 12 Pressure fluctuations as recorded at $(x, y) = (-1.0, 1.5)$ for the NACA-0012 airfoil at $\alpha = 5°$ (solid line) alongside the same pressure signal plotted for frequencies $0 < f < 2$ (dashed line) and $9 < f < 20$ (dotted line).**

The acoustic pressure was stored every 10 iterations, skipping every fourth point in $\xi$ and $\eta$, and the primitive variables $u_i$ and $p$ were also stored within the airfoil boundary layer every 10 iterations, skipping every fourth point in $\xi$ and $\eta$. A preliminary comparison of correlations between acoustic pressure and either $u$, $v$, $w$ or $p$ found pressure/pressure correlations to yield the clearest results, and hence the correlations presented here are all of this form. To avoid self-correlation to acoustic fluctuations within the boundary layer it would be desirable to correlate acoustic pressure to vorticity. Unfortunately, due to the reduced spatial resolution of the time-dependent data capture it is not possible to compute vorticity a posteriori.

### A. Results and Discussion

The three airfoil flows exhibit fundamental similarities in terms of physical phenomena and flow topology. Accordingly, the important conclusions drawn in this section hold for all three flows. Although cross correlations have been performed using data from all three simulations, results will primarily be shown from the NACA-0012 airfoil case at $\alpha = 5°$, for the sake of brevity.

#### *1. Quantifying Self-Correlation of Acoustic Waves*

A variety of acoustic and hydrodynamic behaviors are present for these airfoil flows. In terms of hydrodynamic behavior we expect the upper-surface pressure to be affected by phenomena such as hydrodynamic instability waves, transition to turbulence and the passage of turbulent structures. In terms of acoustic behavior, we expect the surface pressure to be influenced by the passage of acoustic waves originating not only at the airfoil trailing edge, but also in the transition and reattachment regions. The correlation of the acoustic signal at the observer location with the passage of acoustic waves over the airfoil itself must be accounted for if the correlation maps are to be interpreted correctly. Before interpreting the correlation map obtained from the upper surface, it is helpful to first discuss the lower-surface correlation map.

The cross correlation between pressure recorded at an observer location at $(x_o, y_o) = (0.5, -1.5)$ and source locations on the lower airfoil surface is illustrated in Fig. 13 for all frequencies. Also plotted is the mean acoustic-propagation time from the source location to the observer location. Correlation data on this line are the most significant in terms of correlating acoustic behavior at $(x_o, y_o) = (0.5, -1.5)$ to hydrodynamic behavior at the source locations. The lower airfoil surface is subject to a favorable pressure gradient for the extent of the chord and hence remains laminar. This means that the lower-surface pressure fluctuations are primarily caused by the passage of acoustic waves. Furthermore, while trailing-edge noise will radiate below the airfoil, noise generated in the transition/reattachment region will not. Effectively, the cross-correlation map illustrates the self-correlation between trailing-edge noise recorded at $(x_o, y_o) = (0.5, -1.5)$ and trailing-edge noise recorded at the airfoil surface.

It can be seen that the dominant feature of the correlation map is a region of strong positive correlation, present for the extent of the airfoil chord. The region of positive correlation intercepts the mean acoustic-propagation line at $x \approx 1.0$, which confirms that this region is associated with noise originating at the airfoil trailing edge. The fact that the region of positive correlation is inclined with a positive slope and that the retarded time decreases with distance from the

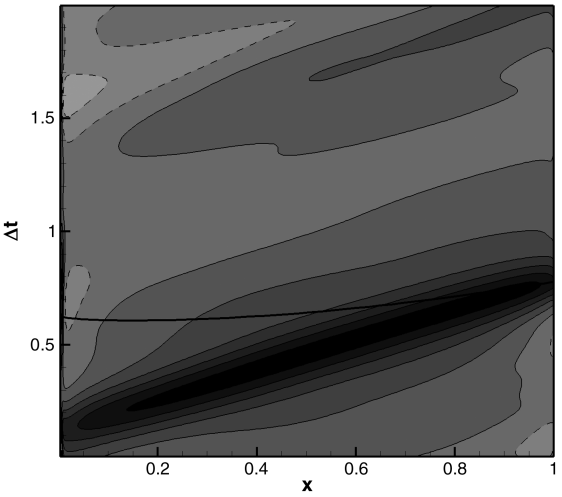


**Fig. 13 Cross correlation between pressure recorded at $(x_o, y_o) = (0.5, -1.5)$ and pressure recorded at the airfoil surface for all frequencies, plotted using 12 levels over the range $C_{pp} = \pm 0.9$. Negative contour lines are shown dashed and the solid line represents the mean acoustic-propagation timeline.**

trailing edge, is consistent with the upstream propagation of acoustic waves. The gradient of the positive correlation region provides an estimate of the propagation velocity. Noting that the axes are intercepted at approximately $(x, \Delta t) = (0, 0.13)$ and $(x, \Delta t) = (1.0, 0.79)$, the propagation velocity is estimated at $u_p = 1.52$, which appears feasible given that for $u_\infty = 1.0$ and $M = 0.4$ (i.e., $c = 2.5$) we would expect a velocity of $u_p = c - u_\infty$ (i.e., $u_p = 1.5$).

*2. High-Pass Cross Correlations to Surface Pressure*

In Sec. III.C.2 frequencies in the range $2.5 < f < 15$ were determined to be of particular interest with respect to the hydrodynamic and behavior response of the airfoil flows. For the purposes of investigating acoustic sources associated with the turbulent flow, it is therefore useful to compute cross-correlation maps omitting low frequencies. The cross correlation between pressure recorded at the observer location $(x_o, y_o) = (0.5, 1.5)$ and the upper-surface pressure is plotted in Fig. 14 (left), for frequencies $f > 2$. It can be seen that there is a complex spatiotemporal structure. There are two locations exhibiting large correlation magnitude. The first lies in the vicinity of $x = 0.2$ and $0 < \Delta t < 0.5$ and takes the form of diagonal-upward-orientated regions of alternating positive and negative correlation. The second is a pair of diagonal-downward-orientated regions with positive and negative correlations that lie across the region $0.5 < x < 1$ and intercept $\Delta t \approx 0.8$ at the airfoil trailing edge.

The diagonal-downward regions intercept the mean acoustic-propagation timeline at the airfoil trailing edge, which strongly suggests that this feature is associated with trailing-edge noise production. Moving away from the trailing edge, the $\Delta t$ associated with this feature increases with respect to the mean acoustic-propagation time. It therefore appears that the acoustic signal is correlating with the turbulent structures in the boundary layer before they convect over the trailing edge to produce trailing-edge noise. Effectively, the upstream history of the trailing-edge noise-production mechanism is observed in this manner. Perhaps surprisingly this feature can be tracked upstream until $x \approx 0.2$. If we assume that this feature is associated with the convection of turbulent structures, we can obtain a velocity estimate of the structures from the gradient of the diagonal-down regions present on the correlation map. Noting that the negative structure appears to intercept the axes at $(x, \Delta t) = (0.3, 1.98)$ and $(x, \Delta t) = (1.0, 0.85)$ we obtain a convection velocity of $u = 0.62$, which appears reasonable. The diagonal-upward regions are observable only in the region $0 < x < 0.3$, which lies in the laminar region of the flow. The fact that these regions possess diagonal-upward orientation suggests that acoustic waves are the dominant source of pressure fluctuations in this region. It is also interesting to note that in the region $0.25 < x < 0.45$ the correlation map exhibits spatiotemporal structure possessing comparatively smaller wavelengths. In this laminar separated region strong convective instability growth is expected [31], and it is likely that the correlation map is influenced by this behavior.

Although large correlation magnitudes are observed in the laminar region, it is highly unlikely that this region acts as an acoustic source. To remove regions from the correlation map that are unlikely to radiate noise, the correlation map is multiplied by $\overline{p'p'(x)}/\overline{p'p'}_{\max}$, where $\overline{p'p'(x)}$ is the root-mean-square (rms) pressure observed at the source location and $\overline{p'p'}_{\max}$ is the maximum rms pressure observed across all source locations. Scaling the correlation map with rms source pressure (Fig. 14, right) effectively removes the laminar

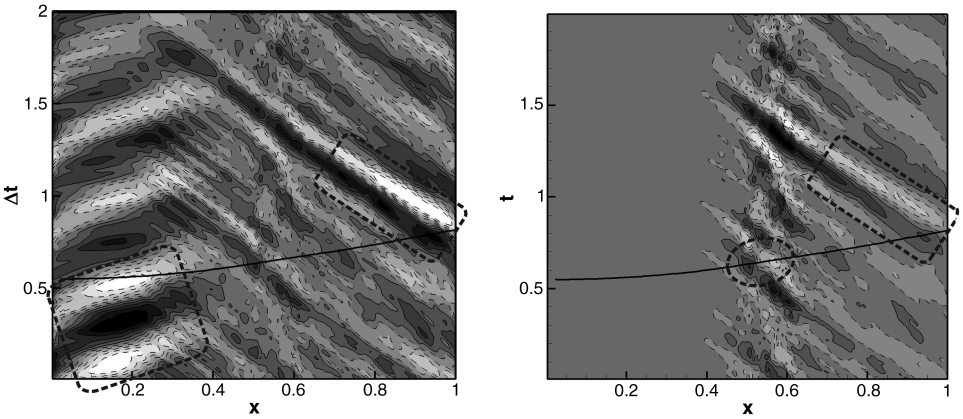


**Fig. 14 Cross correlation between pressure recorded at $(x, y) = (0.5, 1.5)$ and pressure recorded at the airfoil surface for frequencies $f > 2$. Left-hand image is unscaled and shows 10 levels over the range $C_{pp} = \pm 0.3$ whereas right-hand image is scaled with rms surface pressure and shows 10 levels over the range $C_{pp}\overline{p'p'(x)}/\overline{p'p'}_{\max} = \pm 2 \times 10^{-1}$. Negative contour lines are dashed, and thick dashed lines highlight regions discussed in Sec. IV.A.2.**

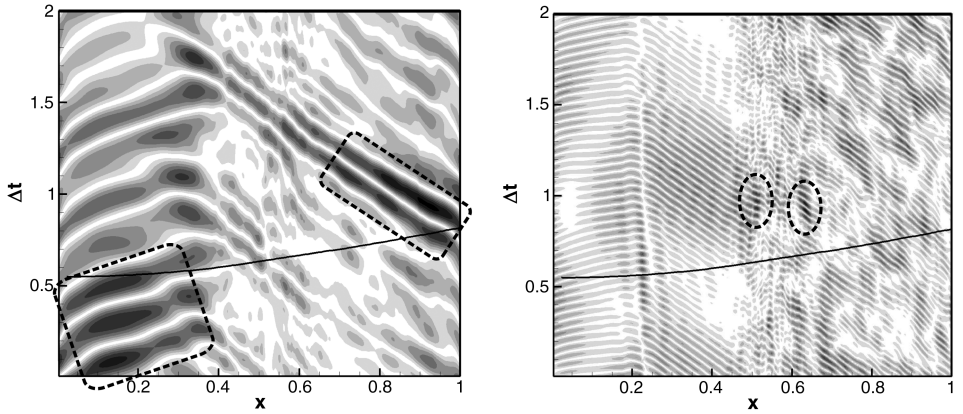


**Fig. 15 Cross correlation between pressure recorded at $(x, y) = (0.5, 1.5)$ and pressure recorded at the airfoil surface for frequencies $2 < f < 6$ showing eight levels over the range $0.06 < \|C_{pp}\| < 0.6$ (left) and for frequencies $9 < f < 20$ showing eight levels over the range $0.037 < \|C_{pp}\| < 0.037$ (right). Dashed lines highlight regions discussed in Sec. IV.A.3.**

region from the correlation map. The diagonal-downward-orientated structure associated with the trailing-edge noise is still present and is the most prominent feature. Correlation levels are also high in the region $0.5 < x < 0.6$, which corresponds to the transition/reattachment region. It is possible that this feature is related to the additional noise sources observed in Sec. III.C; however, it should be noted that this feature did not appear so clearly on the unscaled correlation map.

### 3. *Cross Correlations for Finite-Frequency Bands*

Plotting acoustic pressure for finite-frequency bands suggests that trailing-edge noise is dominant for lower frequencies, while additional noise sources located in the vicinity of transition/reattachment are dominant at higher frequencies (Sec. III.C). In an attempt to isolate these noise sources, cross correlations between acoustic pressure and the upper airfoil surface pressure are computed for two finite-frequency ranges. The first frequency range, $2 < f < 6$, is selected as being the range over which trailing-edge noise is expected to dominate. The second frequency range, $9 < f < 20$, is selected as being the range over which the additional noise sources are expected to dominate. Where correlation maps for finite-frequency ranges are computed, the modulus of the cross correlation is illustrated for clarity.

The correlation map for frequency range $2 < f < 6$ (Fig. 15, left) appears very similar to that obtained for frequencies $f > 2$ (Fig. 14, left), except the smaller wavelength diagonally-downward-orientated features located in the region $0.25 < x < 0.45$ are not present. This suggests that the correlation maps are dominated by the lowest frequency fluctuations present, which will, in general, tend to contain the most energy. Accordingly, the conclusions drawn from this correlation map are the same as those for $f > 2$ (Sec. IV.A.2). In contrast, the correlation map for $9 < f < 20$ appears markedly different. The general structure of this correlation map is similar to those observed previously: diagonal-upward-orientated structures are observed in the laminar region, associated with upstream-propagating acoustic waves, as well as diagonal-downward-orientated structures, associated with downstream-convecting hydrodynamic structures. The cross-correlation map exhibits decreased correlation amplitudes as compared to that for $2 < f < 6$, with less pronounced regions of maxima and minima. In contrast to the previously discussed correlation maps the mean acoustic-propagation timeline does not intersect a region of high-amplitude correlation at the airfoil trailing edge, confirming that the airfoil trailing edge is not a dominant acoustic source for this frequency range. Regions at which the correlation map is greatest in amplitude are offset from the mean acoustic-propagation timeline at $(x, \Delta t) = (0.5, 0.95)$ and $(x, \Delta t) = (0.625, 0.95)$. A possible explanation for these regions of high amplitude is that they are associated with hydrodynamic events that lead to noise production at a later point in time, analogous to the manner in which it is possible to correlate to turbulence about to convect over the airfoil trailing edge and produce noise (Sec. IV.A.2). If this is the case, it is not clear why these regions of high amplitude do not intersect the mean acoustic-propagation line, as will later be shown for other observer locations (Sec. IV.A.5).

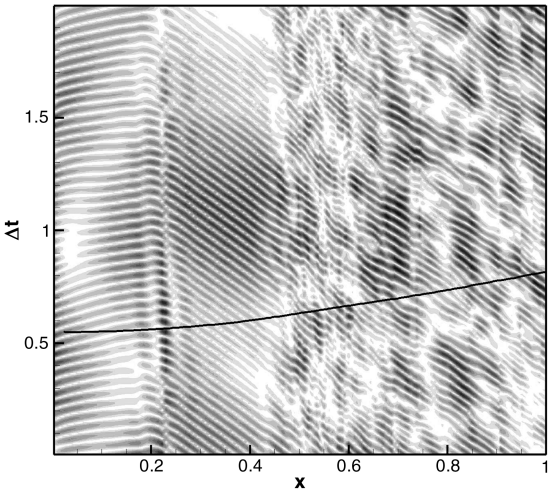


**Fig. 16 Cross correlation between pressure recorded at $(x, y) = (0.5, 1.5)$ and pressure recorded within the upper-surface boundary layer for frequencies $9 < f < 20$ showing 10 levels over the range $0.026 < \|C_{pp}\| < 0.26$.**

### 4. *Cross Correlations to Source Locations Within the Boundary Layer*

The mechanism for noise production in the vicinity of transition/reattachment is not yet known, but turbulent fluctuations in this region are certain to play a primary role. In an effort to more thoroughly investigate behavior in the frequency range $9 < f < 20$, a cross correlation is computed between an observer location at $(x, y) = (0.5, 1.5)$ and source locations within the airfoil boundary layer (as opposed to at the airfoil surface). For each $x$ location, the $y$ coordinate within the boundary layer corresponds to the location of maximum turbulent kinetic energy (TKE). This means that the correlation will include hydrodynamic fluctuations that occur away from the airfoil surface: for example, those associated with transition in the separated shear layer.

The cross-correlation map for source locations within the boundary layer computed for $9 < f < 20$ is plotted in Fig. 16. The correlation map exhibits different regions of correlation maxima/minima as compared to that obtained by correlating to surface pressure. However, the cross correlation again exhibits a more uniform amplitude distribution with no single region of maximum amplitude. In fact, the peak correlation amplitudes observed have decreased from $|C_{pp}| \approx 0.37$ to $\approx 0.26$. Significantly, this means that acoustic radiation in this frequency range correlates more strongly to surface pressure than to pressure associated with turbulent fluctuations within the boundary layer.

### 5. *Effect of Observer Location*

To more thoroughly investigate the additional acoustic sources, the cross correlation between pressure recorded at observer locations $(x, y) = (-1, 1.5)$ and $(x, y) = (1.5, 1.5)$ to pressure recorded upon the upper airfoil surface are illustrated in Fig. 17, for the frequency range $9 < f < 20$. In contrast to the correlation computed for observer location $(x, y) = (0.5, 1.5)$ (Fig. 15, right), the mean acoustic-propagation timeline passes directly through correlation maxima, at $x = 0.75$ for observer location $(x, y) = (-1, 1.5)$ and at $x = 0.65$ for observer location $(x, y) = (1.5, 1.5)$. That the maximum correlation amplitude occurs on the mean acoustic-propagation line for both locations is significant in terms of identifying a physical origin for the additional noise sources. It is also important, however, to note that the maxima do not lie at the same point on the airfoil surface for both observer locations. No local maxima are clearly observed to be associated with trailing-edge noise for either observation location.

### 6. *Surface Pressure Correlations for All Configurations*

Cross correlations between acoustic pressure and the upper-surface pressure for frequency range $9 < f < 20$ yielded potentially enlightening results for the case at $\alpha = 5°$; however, the results were more ambiguous than observed at lower frequencies. To more thoroughly investigate the problem cross correlations are plotted for the for the simulations at $\alpha = 7°$ in Fig. 18, for the frequency range $f < 9 < 20$. These can be compared to the equivalent results at $\alpha = 5°$, in Figs. 3 (left) and 17.

For the NACA-0012 case a region dominated by upstream-traveling acoustic disturbances is present for $0 < x < 0.15$. For the NACA-0006 case, no such region is observed, due to the stronger instability growth rates and more rapid onset of transition. A region of regular coherent downstream-traveling disturbances is present for both cases, appearing consistent with the convection of instability waves. For the NACA-0012 case, this occurs in the range

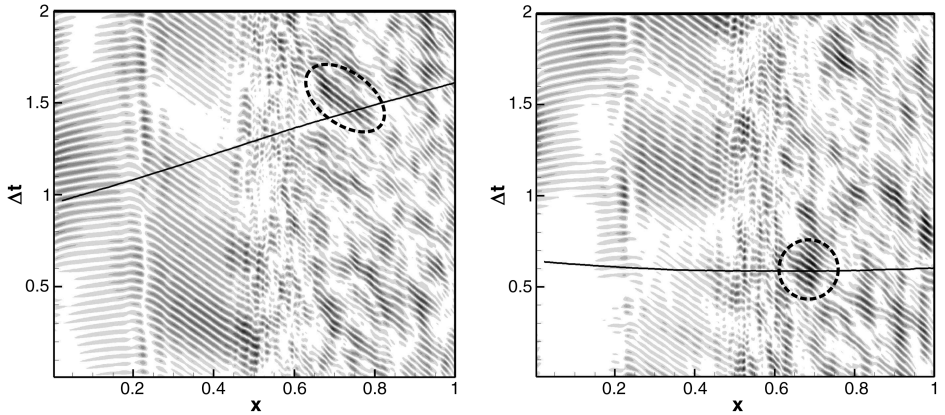


**Fig. 17 Cross correlation between pressure recorded at $(x, y) = (-1.0, 1.5)$ (left) and $(x, y) = (1.5, 1.5)$ (right) and pressure recorded within the upper-surface boundary layer for frequencies $9 < f < 20$ showing 10 levels over the range $0.05 < |C_{pp}| < 0.33$. Dashed lines highlight regions discussed in Sec. IV.A.4.**

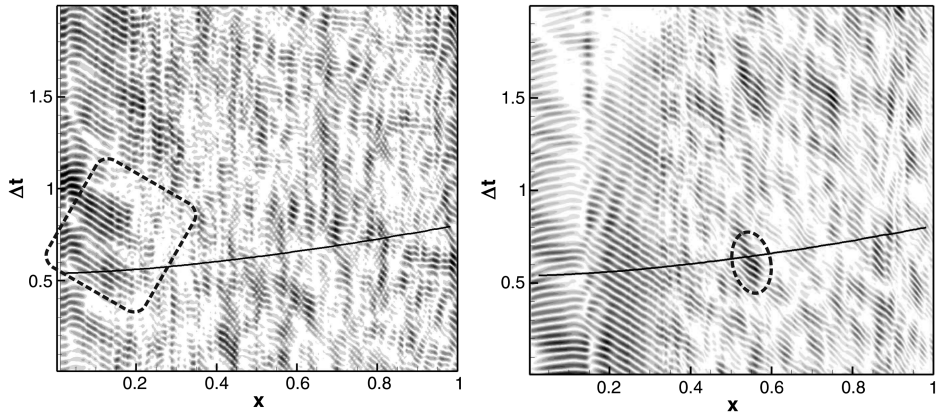


**Fig. 18 Left-hand image shows the cross correlation between pressure recorded at $(x, y) = (0.0, 1.5)$ and pressure recorded at the airfoil surface for the NACA-0006 airfoil at $\alpha = 7°$, showing eight levels over the range $0.05 < |C_{pp}| < 0.37$. Right-hand image shows the cross correlation between pressure recorded at $(x, y) = (0.5, 1.5)$ and pressure recorded at the airfoil surface for the NACA-0012 airfoil at $\alpha = 7°$, showing eight levels over the range $0.05 < |C_{pp}| < 0.29$. Dashed lines highlight regions discussed in Sec. IV.A.**

$0.15 < x < 0.33$, and for the NACA-0006 case, this occurs in the range $0.05 < x < 0.2$. The largest correlation amplitudes for the NACA-0006 case are observed to occur in this region, indicating that the additional noise radiated in this frequency range correlates most strongly to the instability waves driving transition, and there appear to be no other clearly defined regions of maximum correlation. For the NACA-0012 case, correlation amplitudes are again significant in the region where primary instability growth occurs; however, there also appears to be a local correlation maximum located on the mean acoustic-propagation timeline at $x \approx 0.55$.

### B. Discussion of Additional Sources

For the flow around the NACA-0012 airfoil at $\alpha = 5°$ the point at which the separated shear layer reattaches as a turbulent boundary layer is determined to be $x = 0.61$ based on the time-averaged skin-friction distribution. Transition, on the other hand, occurs over a finite streamwise region. Parameters such as the location of minimum skin-friction coefficient ($x = 0.54$, Fig. 19, left) and peak TKE ($x = 0.57$, Fig. 10) provide an indication of the region over which transition occurs for separation-bubble flows. In comparison, cross correlations performed for the frequency range $9 < f < 20$

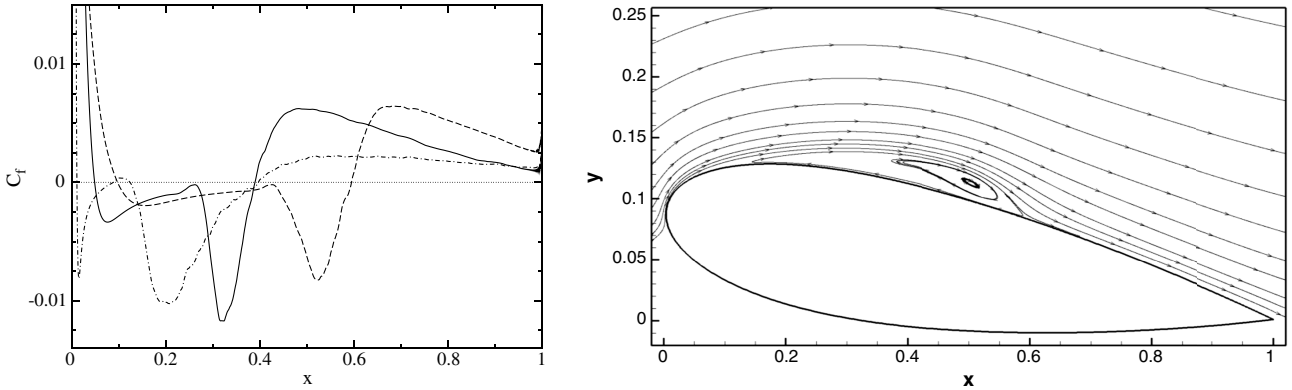


**Fig. 19 Left-hand image shows time-averaged skin-friction coefficient for the NACA-0012 airfoil at $\alpha = 5°$ (solid line), the NACA-0012 airfoil at $\alpha = 7°$ (dashed line) and the NACA-0006 airfoil at $\alpha = 7°$ (dotted–dashed). Right-hand image shows time-averaged streamlines on the upper airfoil surface of the NACA-0012 airfoil at $\alpha = 5°$ (image is shown stretched in the $y$ direction).**

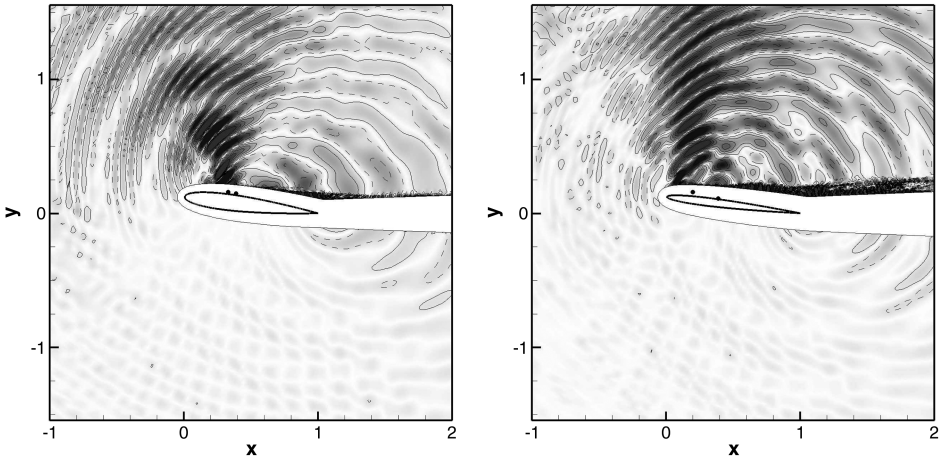


**Fig. 20 Isocontours of the real part of acoustic pressure plotted for $f = 15$ for the NACA-0012 airfoil (left) and NACA-0006 airfoil (right) at $\alpha = 7°$. Black circles indicate the location of maximum TKE and the mean reattachment point.**

exhibit peak values lying upon the mean acoustic-propagation timeline at $x \approx 0.65$ and $x \approx 0.75$ (Fig. 17). Hence, it appears that the acoustic pressure correlates most strongly to the region directly downstream of reattachment. It does not appear possible to distinguish a single location, or point, at which a noise source is dominant. The origin of acoustic waves generated by the additional sources can be hypothesized by considering wave fronts illustrated by plotting the real part of acoustic pressure (Fig. 6). When doing so it should be noted that acoustic waves with the upstream directivity exhibited in Fig. 6 (right) will travel with a greater upstream velocity in the boundary layer (where $u$ is small) as compared to the freestream (where $u$ is large). This is illustrated by the upstream-traveling rays in Fig. 11 (left) and means that if the origin of acoustic waves observed in the freestream (e.g., Fig. 6) is located on the airfoil surface, this origin may be further downstream than one might intuitively suppose. Considering Fig. 6 (right) suggests that the origin of acoustic waves produced by the additional sources lies in the range $0.6 < x < 0.7$. This analysis can be repeated for the two simulations conducted at $\alpha = 7°$ (Table 3). For the NACA-0012 airfoil at $\alpha = 7°$ the transition location is determined to be $x \approx 0.33$. Plotting acoustic pressure at $f = 15$ and visually tracing the wave fronts back to an apparent origin would seem to indicate an acoustic source downstream of the transition location and of the reattachment location (Fig. 20, left); however, the origin of the noise does not appear to be located as far downstream as the cross correlation for this configuration would indicate ($x \approx 0.55$, Fig. 18, right). For the NACA-0006 case at $\alpha = 7°$ the transition location is determined to be $x = 0.2$, and, notwithstanding any upstream acoustic propagation within the boundary layer, the apparent origin of acoustic waves at $f = 15$ appears in this case to lie close to the transition location (Fig. 20, right). There also appears to be a secondary noise source located close to the reattachment point at $x = 0.38$, close to the reattachment point, leading to a discontinuity in the acoustic wave fronts.

It appears then that the behavior of the additional sources is not clearly defined and varies between the configurations presented here. For the NACA-0012 case at $\alpha = 5°$ evidence suggests that the additional noise sources do not radiate directly from the transition region, but instead radiate from a location downstream of the reattachment point. Conversely, for the NACA-0006 case, the additional noise sources appear to radiate from a location much closer to the transition region and to correlate more strongly to instability waves within the boundary layer. The most intuitive hypothesis for the additional noise sources is that the turbulent fluctuations present during transition radiate noise (i.e., as quadrupole sources, with $M^8$ scaling). This appears to be the case for the NACA-0006 airfoil; however, this mechanism would not appear to explain that the origin of the noise radiated at $\alpha = 5°$ appears to be downstream of transition. Turbulent fluctuations in the vicinity of a solid boundary will radiate more efficiently as surface dipoles ($\sim M^6$ scaling), and hence it is also possible that the comparatively weaker turbulent fluctuations present in the boundary layer downstream of transition might act as noise sources. However, if the additional noise was simply due to turbulent fluctuations in the attached boundary layer, acoustic waves would radiate from all locations downstream of reattachment and the noise would be lower in amplitude than that produced at the trailing edge, which is not the case here. Importantly, the separation-bubble flows considered here possess a markedly different topology to attached boundary-layer flows. In contrast to an attached boundary-layer flow, the time-averaged separation bubble exhibits a stagnation streamline corresponding to flow into the airfoil surface (Fig. 10, right, occurring at $x \approx 0.6$). The fact that streamlines immediately downstream of the reattachment point decrease in height from the airfoil surface with streamwise distance will enhance the impingement of more energetic turbulent structures onto the airfoil surface and hence promote noise production via the more efficient dipolar mechanism. Given that the amplitude of turbulent fluctuations in the vicinity of reattachment is significantly higher than that further downstream (Fig. 10), it seems likely therefore that the reattachment region will act as a noise source. It should be noted, however, that the turbulent part of the separation-bubble flow is highly unsteady. Accordingly, the reattachment process is, in fact, highly unsteady, and reattachment is best regarded as occurring over a region rather than a point [14] (the instantaneous skin-friction varies with standard deviation of $8.6 \times 10^{-3}$ about zero for the case at $\alpha = 5°$). Assuming the reattachment process is at least partly responsible for the additional noise sources, this would account for the difficulty in distinguishing a singular location for their physical origin.

Given the above analysis, the question as to why one scenario would exhibit stronger radiation from the reattachment point and one case from the transition region must be answered. First, it is likely that both processes are present for both configurations, but that the dominant noise source appears most prominently in visualizations and cross correlations (which elucidate the largest-amplitude behaviors). Certainly, for the NACA-0006 airfoil there appears to be two noise sources at $f = 15$, one located near the transition location and one located closer to the reattachment location (Fig. 19, right), which appears to corroborate this hypothesis. Second, the flow configurations exhibiting differences appear to correspond to a

**Table 3 Transition location, reattachment location, and location where the maximum correlation to surface pressure is observed for all cases**

| Geometry | $\alpha$ | $x$ location of transition | $x$ location of mean reattachment point | $x$ location of maximum correlation, $9 < f < 20$ |
|---|---|---|---|---|
| NACA-0012 | 5° | 0.55 | 0.61 | 0.70 |
| NACA-0012 | 7° | 0.33 | 0.39 | 0.55 |
| NACA-0006 | 7° | 0.20 | 0.40 | 0–0.2 |

preference for each noise-production mechanism. In contrast to the other flow configurations, the additional noise sources for the NACA-0006 airfoil appear to radiate most strongly from the transition region. This configuration exhibits the greatest amplitude TKE at transition (Fig. 10) and so would be expected to radiate more strongly here. Furthermore, it is apparent from the skin-friction distribution (Fig. 19) that the flow exhibits a weaker reattachment, occurring a greater distance downstream of transition and resulting in smaller-amplitude skin friction in the attached boundary layer. This means that the wall-normal velocity at reattachment (i.e., the flow into the airfoil surface) will be comparatively weaker. In contrast, the case at $\alpha = 5^\circ$ exhibits significantly decreased TKE amplitude in the transition region; however, the TKE amplitude at the reattachment point is greater than that for the NACA-0006 case (0.11 at $x = 0.61$ vs 0.95 at $x = 0.4$), and the reattachment process is more rapid. These differences would be consistent with an increase in noise amplitude generated at the reattachment point.

## V. Conclusions

Direct numerical simulations of the flow around NACA-0006 and NACA-0012 airfoils at incidence were conducted, with the aim of investigating transitional airfoil self-noise. In all cases the upper airfoil surface exhibited laminar separation, transition to turbulence and subsequent reattachment as a turbulent boundary layer. The length of the laminar separation bubble was considerably reduced and the turbulent reattachment location moved upstream in the higher incidence cases: in particular, for the thinner airfoil. The lower airfoil surface remained attached and laminar for the full extent of the airfoil chord for all configurations. Instantaneous contours of the dilatation rates in the vicinity of the airfoils suggest that for all cases the acoustic responses of the airfoil flows are asymmetrical about the chord line. The contribution of trailing-edge noise radiation is significant for low frequencies, while for the highest frequency investigated, the radiated noise appears to be due only to flow events in the transition and reattachment regions on the suction side. For the thinner NACA-0006 airfoil, higher acoustic pressure amplitudes are observed for all frequency ranges, indicating that the airfoil self-noise mechanism is more efficient for this case.

Cross correlations of acoustic pressure in the far field with pressure close to or on the airfoil surface were performed. The trailing-edge noise-production mechanism is clearly observed by computing cross correlations, indicated by regions of large-amplitude correlation located at the trailing edge, at a retarded time associated with acoustic propagation from the source to observer location. This behavior is present for all observer locations investigated. The upstream history of the noise-production mechanism is also observed, in that acoustic pressure at the observer location also correlates to the turbulent boundary-layer input to the trailing-edge noise mechanism.

An attempt was made to identify the origin of the additional noise sources by considering cross correlations over the frequency range $9 < f < 20$, where the additional sources are expected to be dominant. Despite investigating several observer locations, as well as source locations in the boundary layer, it was not possible to determine a single location at which the additional noise sources radiate. Depending on the configuration, the most significant correlation amplitudes were observed either in the region where primary instability growth occurs or else for regions directly downstream of reattachment. Consideration of acoustic wave fronts suggests that the additional sources radiate from the vicinity of transition and from the reattachment region. The turbulent fluctuations present during transition are expected to act as a noise source, radiating via a quadrupole mechanism. The presence of significant turbulent fluctuation amplitudes, in conjunction with stagnation flow into the airfoil surface in the time average, leads to a hypothesis that the reattachment region also acts as a noise source, radiating via a surface dipole mechanism. The inability of cross correlations to identify the additional acoustic source as occurring at a single location, as is possible for trailing-edge noise, is likely to be because the noise-production mechanism takes place over a finite region in the most unsteady part of the flow.

## Acknowledgments

This work was supported by Engineering and Physical Sciences Research Council (EPSRC) grant EP/F048017/1. Part of the computer time was provided by the EPSRC grant GR/S27474/01.

## References

[1] Brooks, T., Pope, D., and Marcolini, M., "Airfoil Self-Noise and Prediction," NASA Ref. Publ. 1218, 1989.

[2] Amiet, R., "Noise Due to Turbulent Flow Past a Trailing Edge," *Journal of Sound and Vibration*, Vol. 47, No. 3, 1976, pp. 387–393. doi:10.1016/0022-460X(76)90948-2

[3] Zhu, W., Heilskov, N., Shen, W., and Sørensen, J., "Modeling of Aerodynamically Generated Noise from Wind Turbines," *Journal of Solar Energy Engineering*, Vol. 127, 2005, p. 517. doi:10.1115/1.2035700

[4] Lutz, T., Herrig, A., Würz, W., Kamruzzaman, M., and Krämer, E., "Design and Wind-Tunnel Verification of Low-Noise Airfoils for Wind Turbines," *AIAA Journal*, Vol. 45, No. 4, 2007, pp. 779–785. doi:10.2514/1.27658

[5] Tam, C. K. W., and Ju, H., "Numerical Simulation of the Generation of Airfoil Tones at a Moderate Reynolds Number," 12th AIAA/CEAS Aeroacoustics Conference, Cambridge, MA, AIAA Paper 2006-2502, May 2006.

[6] Sandberg, R. D., Jones, L. E., and Sandham, N., "Direct Numerical Simulations of Noise Generated by Turbulent Flow over Airfoils," 14th AIAA/CEAS Aeroacoustics Conference, Vancouver, Canada, AIAA Paper 2008-2861, May 2008.

[7] Sandberg, R. D., Jones, L. E., Sandham, N. D., and Joseph, P. F., "Direct Numerical Simulations of Tonal Noise Generated by Laminar Flow Past Airfoils," *Journal of Sound and Vibration*, Vol. 320, No. 4–5, March 2009, pp. 838–858. doi:10.1016/j.jsv.2008.09.003

[8] Roger, M., and Moreau, S., "Back-Scattering Correction and Further Extensions of Amiet's Trailing-Edge Noise Model. Part 1: Theory," *Journal of Sound and Vibration*, Vol. 286, 2005, pp. 477–506. doi:10.1016/j.jsv.2004.10.054

[9] Bouhadji, A., and Braza, M., "Organised Modes and Shock-Vortex Interaction in Unsteady Viscous Transonic Flows Around an Aerofoil Part I: Mach Number Effect," *Computers and Fluids*, Vol. 32, No. 9, 2003, pp. 1233–1260. doi:10.1016/S0045-7930(02)00100-7

[10] Bouhadji, A., and Braza, M., "Organised Modes and Shock-Vortex Interaction in Unsteady Viscous Transonic Flows Around an Aerofoil Part II: Reynolds Number Effect," *Computers and Fluids*, Vol. 32, No. 9, 2003, pp. 1261–1281. doi:10.1016/S0045-7930(02)00101-9

[11] Bourdet, S., Bouhadji, A., Braza, M., and Thiele, F., "Direct Numerical Simulation of the Three-Dimensional Transition to Turbulence in the Transonic Flow Around a Wing," *Flow, Turbulence and Combustion*, Vol. 71, No. 1, 2003, pp. 203–220. doi:10.1023/B:APPL.0000014932.28421.9e

[12] Desquesnes, G., Terracol, M., and Sagaut, P., "Numerical Investigation of the Tone Noise Mechanism over Laminar Airfoils," *Journal of Fluid Mechanics*, Vol. 591, 2007, pp. 155–182. doi:10.1017/S0022112007007896

[13] Shan, H., Jiang, L., and Liu, C., "Direct Numerical Simulation of Flow Separation Around a NACA 0012 Airfoil," *Computers and Fluids*, Vol. 34, No. 9, 2005, pp. 1096–1114. doi:10.1016/j.compfluid.2004.09.003

[14] Jones, L., Sandberg, R., and Sandham, N., "Direct Numerical Simulations of Forced and Unforced Separation Bubbles on an Airfoil at Incidence," *Journal of Fluid Mechanics*, Vol. 602, 2008, pp. 175–207. doi:10.1017/S0022112008000864

[15] Kim, H., Lee, S., and Fujisawa, N., "Computation of Unsteady Flow and Aerodynamic Noise of NACA 0018 Airfoil Using Large-Eddy Simulation," *International Journal of Heat and Fluid Flow*, Vol. 26, No. 2, 2006, pp. 229–242. doi:10.1016/j.ijheatfluidflow.2005.08.007

[16] Marsden, O., Bogey, C., and Bailly, C., "Direct Noise Computation of the Turbulent Flow Around a Zero-Incidence Airfoil," *AIAA Journal*, Vol. 46, No. 4, 2008, p. 874. doi:10.2514/1.29825

[17] Oberai, A., Roknaldin, F., and Hughes, J., "Computation of Trailing-Edge Noise Due to Turbulent Flow over an Airfoil," *AIAA Journal*, Vol. 40, No. 11, 2002, pp. 2206–2216. doi:10.2514/2.1582

[18] Terracol, M., Manoha, E., Herrero, C., Labourasse, E., Redonnet, S., and Sagaut, P., "Hybrid Methods for Airframe Noise Numerical Prediction," *Theoretical and Computational Fluid Dynamics*, Vol. 19, No. 3, 2005, pp. 197–227.
doi:10.1007/s00162-005-0165-5

[19] Shen, W., Zhu, W., and Sørensen, J., "Aeroacoustic Computations for turbulent Airfoil Flows," *AIAA Journal*, Vol. 47, No. 6, 2009, pp. 1518–1527.
doi:10.2514/1.40399

[20] Bogey, C., and Bailly, C., "Computation of a High Reynolds Number Jet and Its Radiated Noise Using Large Eddy Simulation Based on Explicit Filtering," *Computers and Fluids*, Vol. 35, No. 10, 2006, pp. 1344–1358.
doi:10.1016/j.compfluid.2005.04.008

[21] White, F. M., *Viscous Fluid Flow*, McGraw–Hill, New York, 1991.

[22] Carpenter, M. H., Nordström, J., and Gottlieb, D., "A Stable and Conservative Interface Treatment of Arbitrary Spatial Accuracy," *Journal of Computational Physics*, Vol. 148, No. 2, Jan. 1999, pp. 341–365.
doi:10.1006/jcph.1998.6114

[23] Sandham, N., Li, Q., and Yee, H., "Entropy Splitting for High-Order Numerical Simulation of Compressible Turbulence," *Journal of Computational Physics*, Vol. 178, 2002, pp. 307–322.
doi:10.1006/jcph.2002.7022

[24] Sandberg, R. D., Sandham, N. D., and Joseph, P. F., "Direct Numerical Simulations of Trailing-Edge Noise Generated by Boundary-Layer Instabilities," *Journal of Sound and Vibration*, Vol. 304, No. 3–5, July 2007, pp. 677–690.
doi:10.1016/j.jsv.2007.03.011

[25] Sandhu, H., and Sandham, N. D., "Boundary Conditions for Spatially Growing Compressible Shear Layers," Rept. QMW-EP-1100, Faculty of Engineering, Queen Mary and Westfield College, Univ. of London, London, 1994.

[26] Sandberg, R. D., and Sandham, N. D., "Nonreflecting Zonal Characteristic Boundary Condition for Direct Numerical Simulation of Aerodynamic Sound," *AIAA Journal*, Vol. 44, No. 2, Feb. 2006, pp. 402–405.
doi:10.2514/1.19169

[27] Drela, M., and Giles, M., "Viscous-Inviscid Analysis of Transonic and Low Reynolds Number Airfoils," *AIAA Journal*, Vol. 25, No. 10, 1987, pp. 1347–1355.
doi:10.2514/3.9789

[28] von Terzi, D. A., "Numerical Investigation of Transitional and Turbulent Backward-Facing Step Flows," Ph.D. Thesis, Univ. of Arizona, Tucson, AZ, 2004.

[29] Spalart, P. R., "Direct Simulation of a Turbulent Boundary Layer up to $R_\theta = 1410$," *Journal of Fluid Mechanics*, Vol. 187, 1988, pp. 61–98.
doi:10.1017/S0022112088000345

[30] Jones, L., Sandberg, R., and Sandham, N., "Stability and Receptivity Characteristics of a Laminar Separation Bubble on an Aerofoil," *Journal of Fluid Mechanics*, Vol. 648, 2010, pp. 257–296.
doi:10.1017/S0022112009993089

[31] Jones, L. E., "Numerical Studies of the Flow Around an Airfoil at Low Reynolds Number," Ph.D. Thesis, Univ. of Southampton, Southampton, England, U.K., 2007.

[32] Hu, Z., Morfey, C., and Sandham, N., "Sound Radiation in Turbulent Channel Flows," *Journal of Fluid Mechanics*, Vol. 475, 2003, pp. 269–302.
doi:10.1063/1.2337733

[33] Yang, Z., and Voke, P., "Large-Eddy Simulation of Boundary-Layer Separation and Transition at a Change of Surface Curvature," *Journal of Fluid Mechanics*, Vol. 439, 2001, pp. 305–333.
doi:10.1017/S0022112001004633

[34] Rinoie, K., and Takemura, N., "Oscillating Behaviour of Laminar Separation Bubble Formed on an Aerofoil Near Stall," *The Aeronautical Journal*, Vol. 108, No. 1081, 2004, pp. 153–163.

[35] Candel, S., "Acoustic Conservation Principles and an Application to Plane and Modal Propagation in Nozzles and Diffusers," *Journal of Sound and Vibration*, Vol. 41, No. 2, 1975, pp. 207–232.
doi:10.1016/S0022-460X(75)80098-8

A. Lyrintzis
*Associate Editor*